Detection of Mechanical Deformation Induced by Ultrafast Laser Irradiation Upon a Metallic Cantilever

Takuto Ichikawa,* Aizitiaili Abulikemu, and Muneaki Hase†
Department of Applied Physics, Faculty of Pure and Applied Sciences, University of Tsukuba, 1-1-1 Tennodai, Tsukuba 305-8573, Japan

(Received 30 June 2022; revised 21 September 2022; accepted 23 December 2022; published 21 February 2023)

In the work presented here, we systematically investigate the ultrafast optical properties of aluminum (Al) thin films on silicon cantilevers using a microscopic femtosecond optical pump-probe technique to explore the effect of light irradiation upon cantilevers while considering radiation-pressure and photothermal effects. The ultrafast laser pulses used for the study are less than 30 fs in duration and 830 nm in wavelength, and the photon energy (1.49 eV) of the light pulses is close to the interband transition threshold (ITT) of Al. Therefore, the change in the ITT due to the strain in the cantilever induced by the light irradiation can be detected through a change in the transient reflectivity, which is dominated by the thermalized electron signal. We reveal the position dependence of the transient-reflectivity change and the thermalized-electronic-signal amplitude for 100-nm-thick Al films on cantilevers of length 160, 200, and 240 μm, and these results are in excellent agreement with two-temperature-model-based curve fits. Furthermore, to understand the effect of light irradiation, we derive equations for the position-dependent radiation-pressure effect and the photothermal effect, and demonstrate that thermal-expansion-induced changes in the ITT dominate the position dependence of the signal intensity. Our findings offer avenues for exploring the effects of strain on ultrafast properties, and applications to ultrafast scanning probe microscopy.

DOI: 10.1103/PhysRevApplied.19.024054

I. INTRODUCTION

The irradiation of a material by a pulsed laser is associated with not only elementary excitations such as carriers and phonons but also phenomena such as photothermal [1] and radiation-pressure effects [2], involving mechanical deformation of the material. The photothermal effect, a phenomenon where a part of the absorbed light energy is converted into heat, has been discussed as a laser ablation mechanism [3] and is the reason for the thermal expansion of the tip in time-resolved scanning tunneling microscopy (STM) or atomic force microscopy (AFM) [4,5]. The radiation-pressure effect, proposed by Maxwell [6], is understood to be caused by light imparting momentum to matter. When a photon is reflected or absorbed by a material, a change in momentum occurs, resulting in a pressure [7,8]. Sunlight can produce a radiation-pressure effect, and its influence on the position control of the spacecraft Hayabusa has been discussed [9,10]. Moreover, ultrafast laser-induced radiation pressure has been applied as an optical-tweezers technique to manipulate nanomaterials and has been attracting increasing attention recently [11].

On the other hand, AFM is often used to observe photothermal and radiation-pressure effects. Ma *et al.* separated photothermal and radiation-pressure effects by examining the resonant frequency of a cantilever [12]. Several other studies have been reported [13,14], although those experiments were mainly based on existing AFM systems using continuous-wave (cw) lasers. However, the possibility of observing ultrafast laser-induced photothermal and radiation-pressure effects on a cantilever in more advanced time-resolved STM (or AFM) has rarely been investigated [15]. Therefore, as a step toward femtosecond time-resolved AFM, we attempt to observe photothermal and radiation-pressure effects on aluminum (Al)-coated silicon cantilevers under femtosecond pulsed laser irradiation.

Optical pump-probe techniques have achieved high temporal resolution using ultrafast pulsed lasers and have been used as experimental methods for investigating ultrafast relaxation dynamics of quasiparticles, such as in the cases of electron-hole plasmas, coherent phonons, and coherent spins in various materials such as nonmagnetic [16,17] and magnetic [18,19] metals, and semiconductors [20–22]. Optical excitation from equilibrium to nonequilibrium states is followed by relaxation processes, during which electron-electron scattering, electron-phonon scattering, and phonon-phonon scattering occur [23]. For simple metals, the very high density of free electrons causes rapid damping of the electron coherence, thereby

*s2130052@s.tsukuba.ac.jp
†mhase@bk.tsukuba.ac.jp

 © 2023 American Physical Society

dominating the incoherent electron-phonon scattering during the relaxation processes [24]. Under such conditions, simplified models for describing the thermalization dynamics by considering independently thermalized energy distributions that can be characterized by temperatures in the electron and lattice subsystems can be used to make predictions that can be compared with experimental data [25]. Furthermore, a two-temperature model (TTM) for a coupled system of electrons and a lattice has been used for modeling the dynamics in a simple metal [26–29]. Recently, more complex models based on the TTM have been produced by considering temperature gradients [30], phonon dispersion curves [31], and spin systems [32], and by introducing a nonequilibrium Green's function method [33,34]. However, the TTM has not been applied to explore radiation-pressure and photothermal effects on a simple metal.

Al provides a good example of a TTM-based description of electron thermalization because of the fast lattice equilibration caused by the significant phonon anharmonicity, characterized by a large phonon-phonon linewidth [27]. These characteristics make Al a suitable medium for femtosecond plasmonic applications of surface-plasmon-polariton waves [35] and plasmon enhancement at a cantilever tip in ultrafast scattering-type scanning nearfield optical microscopy (s-SNOM) [36]. However, heat accumulation in cantilever tips due to femtosecond pulsed laser irradiation remains a fundamental problem in ultrafast scanning-probe-microscopy techniques such as ultrafast s-SNOM [36], and experimental exploration of the interaction between femtosecond pulsed lasers and cantilevers to solve this problem has been lacking.

In this study, we use a thin Al film on a cantilever as an example of a metallic system where ultrafast dynamics after pulse excitation can be appropriately reproduced using the TTM. Ultrashort laser pulses from a mode-locked Ti:sapphire oscillator with a center wavelength of 830 nm (1.49 eV) are used as the excitation and probe light. The pulse width of the optical excitation is shorter than the electron thermalization time constant (approximately 200 fs), and under ultrafast excitation, we observe transient coherent signals from the sample. We observe a remarkable position dependence of the transient-reflectivity change ($\Delta R/R$) on an ultrafast timescale. Moreover, we investigate the effects of light irradiation in terms of the position-dependent radiation-pressure and photothermal properties of the Al film on the cantilever, and find that the strain originates mainly from the photothermal effect and shows considerable position dependence of the $\Delta R/R$ signal.

II. EXPERIMENTS

We perform a reflective pump-probe experiment on an Al film on a cantilever in the field of view of a microscope using the measurement system shown in Fig. 1(a). The

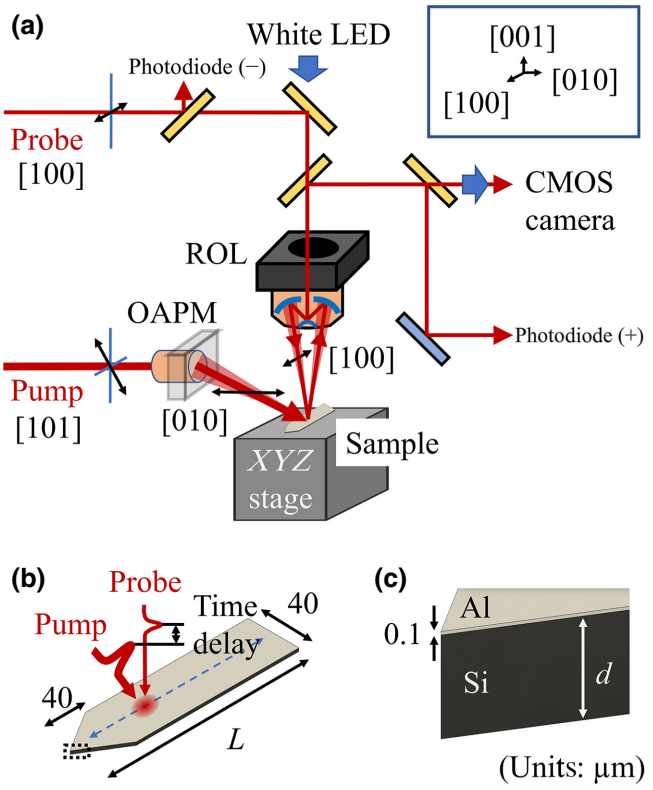

FIG. 1. (a) Simplified scheme of the optical setup for the microscopic femtosecond optical pump-probe measurements. Each yellow rectangle represents a beam splitter. Each orange cylinder represents a focusing component, which is an off-axis parabolic mirror (OAPM) or a reflective objective lens (ROL). (b) Enlarged view around the sample (the Al-coated Si cantilever) in (a). (c) Enlarged view of the area enclosed by the black dotted line in (b). L and d represent the length and thickness, respectively, of the cantilever.

light source used is a mode-locked Ti:sapphire laser with a central wavelength of 830 nm (photon energy $\hbar\omega = 1.49$ eV), a pulse width τ_p less than 30 fs, and a repetition rate f_{rep} of 80 MHz. The laser pulse is split into strong pump and weak probe pulses using a beam splitter, and these pulses travel along different optical paths. The time delay between the pump and probe pulses is scanned at a frequency of 19.5 Hz and an amplitude of 15 ps using an oscillating retroreflector.

All measurements are performed at room temperature, T_0 (approximately 300 K). Notably, an off-axis parabolic mirror (OAPM) and a reflective objective lens (ROL) are used as reflective-focusing components instead of transparent lenses to minimize the group-velocity dispersion effects on the pulsed light, and improve the temporal resolution of the measurements. The pump and probe pulses are focused using an OAPM (the depression angle is approximately 45°) and a ROL with focal lengths of 50.8 and 13.3 mm, respectively. The shape of the laser spot can be

observed in microscope images when the sample is opaque and has a relatively low reflectivity, such as in the case of a GaAs wafer. Therefore, we observe the Gaussian shape of the focal spots of both pulses on GaAs and obtain spatial overlap to detect a signal from excited carriers using pump-pulse irradiation of the GaAs surface. The pump power is controlled at approximately 154 mW, and the shape of the pump beam is made nearly circular by adjusting the tilt angle of the kinematic mount of the OAPM. Finally, an oval spot of pump light with major and minor axes of 21.1 and 14.4 μm, respectively, for the $1/e^2$ width of the Gaussian function is demonstrated by microscope images, and the corresponding optical fluence is approximately 800 $\mu J/cm^2$. Similarly, the size of the probe spot is measured to be 6.6 and 4.2 μm for the major and minor axes, respectively. The polarizations of the focused pump and probe light are orthogonal each other to minimize the effect of the background signal caused by scattered pump light. Since the direction of the wave vector **k** of the pump light reflected from the OAPM is $[\bar{1}0\bar{1}]$, [010] can be selected as the direction of polarization. This polarization condition can be realized by using [101]-polarized pump light incident on the OAPM. The energy of the photons in the pulse is close to the interband transition threshold (ITT) [37–39], which enables us to observe a large signal in the form of a reflectivity change (divided by the reflectivity without optical excitation) $\Delta R/R$.

Our experimental setup enables us to observe real-time voltage signals related to ultrafast reflectivity changes on a digital oscilloscope after an appropriately amplified and filtered photocurrent signal is detected by a pair of photodiodes, as shown in Fig. 1(a). The photocurrent signal ΔI equals the value of the current detected by one photodiode (−), I_-, subtracted from the current detected by the other photodiode (+), I_+. All measurements are performed after maximizing the value ΔI (proportional to ΔR) by monitoring the voltage signal, and the normalized reflectivity change $\Delta R/R$ is constructed by normalization of ΔI by I_+ (proportional to R) to give $\Delta I/I_+ (= \Delta R/R)$.

Three Al-coated Si cantilevers, whose lengths L are 160, 200, and 240 μm, are the samples used [Fig. 1(b)]. The respective dimensions (width w and thickness d) and mechanical properties (resonant frequency f_0 and spring constant k_z) of the cantilevers are listed in Table I. Al is used as the reflective metal coating to detect the deflection [40]. As illustrated in Fig. 1(c), the thickness of the Al film is estimated to be approximately 100 nm using a focused ion-beam system, whose highest spatial resolution is 5 nm. These cantilevers are carefully attached to the same sample holder to maintain horizontal accuracy, which is confirmed by observing a uniformly focused laser beam in a microscope image. Each cantilever is attached along the [100] direction, and the sampling position is controlled along the same direction during the measurements.

TABLE I. Length L, width w, thickness d, resonant frequency f_0, and spring constant k_z of the three Al-coated Si cantilevers used in the experiments.

L (μm)	w (μm)	d (μm)	f_0 (kHz)	k_z (N/m)
160	40	3.7	280	25
200	40	3.5	150	12
240	40	2.3	73	2.2

III. RESULTS AND DISCUSSION

A. Fitting based on two-temperature model

The coupled differential equations using the TTM to describe the dynamics of the electron (T_e) and lattice (T_l) temperatures in an Al thin metallic film are given by

$$C_e(T_e)\frac{\partial T_e}{\partial t} = -G(T_e - T_l) + P(t) \tag{1a}$$

and

$$C_l\frac{\partial T_l}{\partial t} = G(T_e - T_l), \tag{1b}$$

where $P(t)$ is the absorbed energy density, $C_e(T_e)$ is the heat capacity of the electrons, C_l is the heat capacity of the lattice, and G is the electron-phonon coupling constant [25,41]. $C_e(T_e)$ can be approximated by a simple linear dependence on T_e using $C_e = \gamma T_e$ in the range of electron temperatures obtained in our experiments ($T_e <$ 2000 K) [41]. γ is the Sommerfeld constant, which is 135 $J\,m^{-3}\,K^{-2}$ in Al [41]. C_l is found to be almost constant, at 2.30×10^6 $J\,m^{-3}\,K^{-1}$ around room temperature, using the Debye temperature (428 K) of Al [41]. In addition, the value of G is nearly constant (2.45×10^{17} $W\,m^{-3}\,K^{-1}$) at T_0 [41]. For an expression for $P(t)$, a temporally Gaussian-shaped pulse is commonly used to obtain

$$P(t) = \frac{(1-R)F_p}{\delta\tau_p}\exp\left(-\frac{t^2}{\tau_p^2}\right), \tag{2}$$

where F_p is the pump fluence, δ is the optical penetration depth, and τ_p is the laser pulse width. A value of $\delta =$ 9.65 nm at the central wavelength of 830 nm [42] is used for simulating our experimental conditions. Using $F_p =$ 800 $\mu J/cm^2$ and $\tau_p = 30$ fs to numerically solve Eqs. (1a) and (1b), we obtain a maximum value of $\Delta T_e \sim 1700$ K. For $T_e <$ 2000 K, the assumption $C_e = \gamma T_e$ is valid, and the time scale of thermalization of the electrons and lattice is comparable to that of the experimental results (approximately 1.0 ps). However, the observed initial coherent signal cannot be reproduced by Eqs. (1a) and (1b) (data not shown), suggesting that an additional term related to non-thermal (NT) electrons needs to be used to reproduce faster relaxation signals. Sun *et al.* [25] introduced NT terms, and

analytical solutions were derived when $C_e \ll C_l$ and C_e and G are constants:

$$N \propto H(t) \exp\left(-\frac{t}{\tau_{\rm NT}}\right), \tag{3a}$$

$$C_e \Delta T_e \propto \Delta T_e \propto H(t)\left[1 - \exp\left(-\frac{t}{\tau_{\rm th}}\right)\right]\exp\left(-\frac{t}{\tau_{\rm ep}}\right), \tag{3b}$$

where N is the energy density stored in the NT electron distribution, $H(t)$ is the Heaviside step function, $\tau_{\rm NT}$ is the decay time of the NT electron population, and $\tau_{\rm th}$ and $\tau_{\rm ep}$ are the rise and decay times, respectively, of the thermalized electron population [25].

Since C_e $(= \gamma T_e)$ is no longer constant for the large change in T_e from 300 to 2000 K, we introduce a stretch coefficient α_s into Eq. (3b), considering the T_e dependence of C_e [41]. Finally, introducing error functions in the form of the convolution of $H(t)$ and a Gaussian function with a width of τ_p and a background (BG), the fitting function for our experiments can be expressed as

$$\begin{aligned}\frac{\Delta R(t)}{R} = {} & \frac{A_{\rm NT}}{2}\left[{\rm erf}\left(\frac{t-t_0}{\tau_p}\right)+1\right]\exp\left(-\frac{t-t_0}{\tau_{\rm NT}}\right) \\ & + \frac{A_{\rm th}}{2}\left[{\rm erf}\left(\frac{t}{\tau_p}\right)+1\right] \\ & \times\left\{1-\exp\left[-\left(\frac{t}{\tau_{\rm th}}\right)^{\alpha_s}\right]\right\} \\ & \exp\left[-\left(\frac{t}{\tau_{\rm ep}}\right)^{\alpha_s}\right] + O(t^3),\end{aligned} \tag{4}$$

where $A_{\rm NT}$ and $A_{\rm th}$ are the NT and thermalized electronic signal amplitudes, respectively, and $O(t^3)$ is the BG term, assuming a cubic function. We confirm the validity of the fitting function by applying it to the measured $\Delta R(t)/R$ signal from a 100-nm-thick Al film on stable fused silica, as shown in Fig. 2. The fit result is satisfactory, and we obtain the parameters $A_{\rm NT} = (711 \pm 3) \times 10^{-6}$, $\tau_p = 38.3 \pm 0.1$ fs, $\tau_{\rm NT} = 22.8 \pm 0.1$ fs, $A_{\rm th} = (195 \pm 3) \times 10^{-6}$, $\tau_{\rm th} = 234 \pm 2$ fs, $\tau_{\rm ep} = 860 \pm 8$ fs, $t_0 = 125$ fs, and $\alpha_s = 1.32 \pm 0.01$. The same fitting is possible for the Al films on cantilevers shown in the next section. The photoabsorption originating from the parallel band structure of Al, as reported in Ref. [39], dominates the $\Delta R/R$ signal in some recent femtosecond optical pump-probe experiments [26,30,43]; this is also the case in the present study, as discussed below.

The effective crystal potential V_{200} parallel to the (200) plane in Al resolves the degeneracy of the bands. A vertical electronic transition from the lower (E_-) to the higher (E_+) band over the Fermi level occurs for a wave vector between $k_\perp^{(1)}$ and $k_\perp^{(2)}$, as indicated in the inset of Fig. 2 [37–39]. The interband-transition threshold $E_{\rm ITT}$ is approximately equal to $2V_{200}$, and the contribution of this transition to the imaginary part of the dielectric constant ϵ_2 is given by $\epsilon_2(\hbar\omega, E_{\rm ITT}) \propto (\hbar\omega)^{-1}(\hbar\omega - E_{\rm ITT})^{-1/2}$ for $\hbar\omega > E_{\rm ITT}$ [37,39,44]. In the thermalized electron system, since the density of electronic states in the vicinity of the Fermi level can be described by a Fermi distribution with an electron temperature T_e, and the $\Delta R/R$ signal is dominated by the contribution of $\Delta\epsilon_2$ due to the change in the electron temperature ΔT_e, the amplitude of the thermalized electronic signal $A_{\rm th}$ is proportional to the change in $E_{\rm ITT}$, i.e., $A_{\rm th} \propto \Delta T_e \propto \Delta\epsilon_2 \propto \Delta E_{\rm ITT}$.

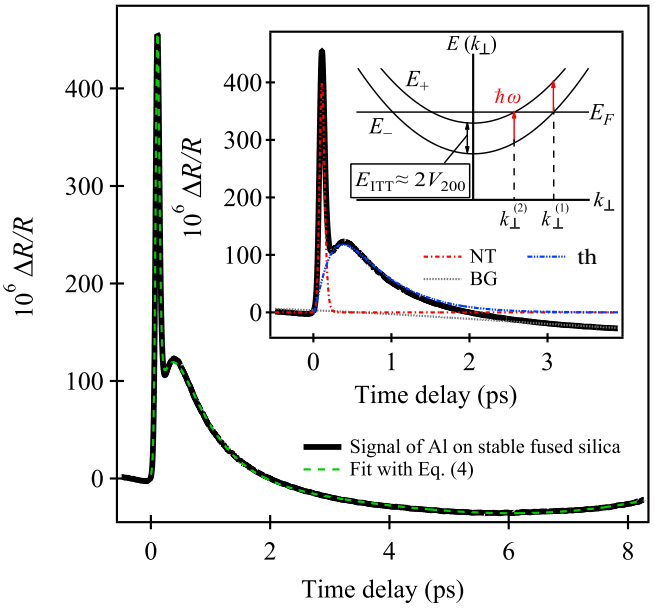

FIG. 2. Transient-reflectivity-change signal $\Delta R/R$ from a 100-nm-thick Al film on stable fused silica. The thick black line represents the raw data, and the green dashed line represents a curve fitted using Eq. (4). The fitting components for the NT electrons [the first term of Eq. (4)], thermalized electrons [the second term of Eq. (4)], and the background [the third term of Eq. (4)] are shown by red, blue, and gray dashed lines, respectively, overlapping the measured signal (thick black line), in the inset. The inset also shows a schematic illustration of the energy bands (the lower band is E_- and the higher band is E_+) mapped in a plane onto the (200) face of the Brillouin zone in Al, based on Ref. [39]. The horizontal black line represents the Fermi level, while the vertical red arrows indicate interband transitions caused by photons with an energy $\hbar\omega > E_{\rm ITT}$.

B. Position-dependent time-domain signals

The position-dependent $\Delta R/R$ signals from the 100-nm-thick Al film on the 240-μm-long cantilever are shown in Fig. 3(a), together with the probe photocurrent I_+ (proportional to R) in Fig. 3(b). The transient-reflectivity-change signal near the root of the cantilever ($\Delta R/R \sim 5 \times 10^{-4}$ for $x = 20$ μm) is at the same level as that for the Al film on a stable substrate shown in Fig. 2. The $\Delta R/R$ signal

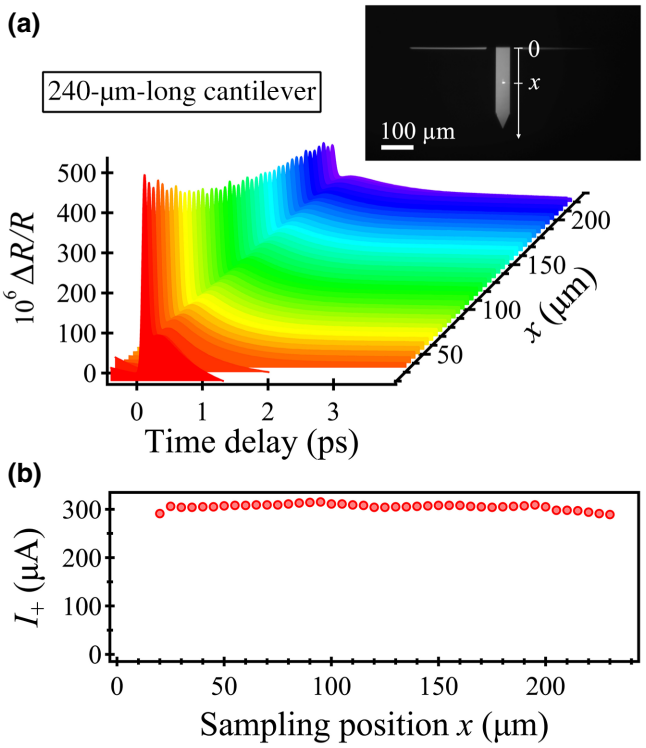

FIG. 3. (a) Position-dependent time-domain $\Delta R/R$ signals from a 100-nm-thick Al film on a 240-μm-long cantilever. The sampling position x (μm) is expressed as the distance from the root of the cantilever. Forty-three signals are aligned, from $x = 20$ (front) to $x = 230$ (back). The smallest (largest) value of x is determined by the limit of accurate measurement because of scattering of the pump spot from the root (end) of the cantilever. (b) Value of the position-dependent current I_+ used for normalization of ΔI (proportional to ΔR).

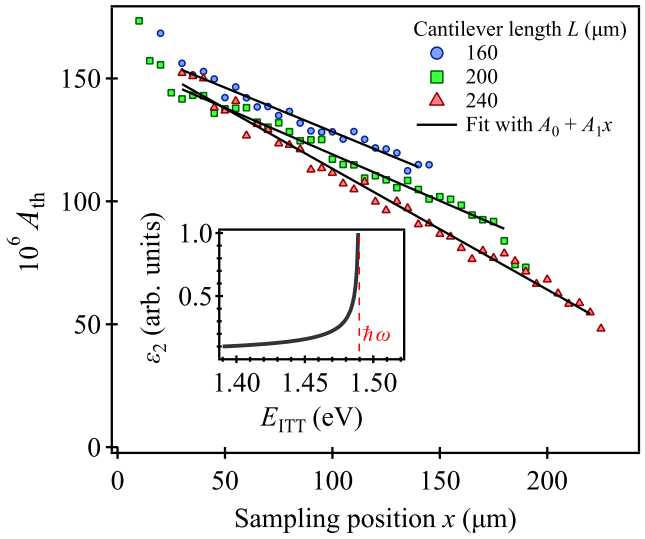

FIG. 4. Position dependence of the thermalized-electronic-signal amplitude $A_{\rm th}$ obtained from 100-nm-thick Al films on 160-, 200-, and 240-μm-long cantilevers, shown by blue circles, green squares, and red triangles, respectively. The black lines represent linear-function fits ($A_0 + A_1 x$) in the range $30 \le x \le L - 20$. The inset presents the imaginary part of the dielectric constant $\epsilon_2(\hbar\omega, E_{\rm ITT}) \propto (\hbar\omega)^{-1}(\hbar\omega - E_{\rm ITT})^{-1/2}$, with $\hbar\omega = 1.49$ eV, as a function of $E_{\rm ITT}$.

gradually decreases as the sampling position shifts from the root to the endpoint of the cantilever [see Fig. 3(a)]. We perform the same measurements on the 200- and 160-μm-long cantilevers, and confirm similar tendencies, indicating that the phenomena observed in Fig. 3 are common. This means that the dramatic decrease in the $\Delta R/R$ signal cannot be explained by a change in the static reflectivity R at different positions, as discussed below.

Each signal is fitted by using Eq. (4), and the results for the position dependence of the fitting coefficients $A_{\rm th}$ are shown in Fig. 4. All parameters are successfully extracted using the curve fitting. In Fig. 4, we find a clear position dependence reflected in the thermalized-electronic-signal amplitude $A_{\rm th}$, and the same dependence is observed for all three cantilevers. This is attributed to the position dependence of ΔR because the values of I_+ (proportional to R) obtained at different sampling positions are nearly constant (the fluctuation is less than 10%), as shown in Fig. 3(b). To compare the rates of decrease of $A_{\rm th}$, we fit the data using a linear function $A_0 + A_1 x$, where A_0 is the constant for $x = 0$ and A_1 is the variation with respect to x. Furthermore, we select the fitting range $30 \le x \le L - 20$, since the experimental errors near the root of the cantilever largely prevent us obtaining precise values for A_0 and A_1. The same fitting is also performed for the other parameters ($A_{\rm NT}$, τ_p, $\tau_{\rm NT}$, $\tau_{\rm th}$, and $\tau_{\rm ep}$), and the results are shown in Appendix A. Although t_0 and α_s do not show a linear trend, the values (t_0, 125–150 fs; α_s, 1.4–1.5) are close to the fit results for the Al film on stable fused silica (data not shown). It is notable that the electron-thermalization time constant $\tau_{\rm th}$ (approximately 200 fs) obtained from the cantilevers is sufficiently longer than the pulse length τ_p (approximately 30 fs) to allow separation of the NT and thermalized electronic signals.

Next, to clarify the mechanism of the linear position dependence of the thermalized-electron-signal amplitude $A_{\rm th}$ (proportional to $\Delta E_{\rm ITT}$), we investigate the main position-dependent effects on the cantilever: the radiation-pressure effect and the photothermal effect [12]. However, under our experimental conditions, the pump and probe beams irradiate the same position at a repetition rate of 80 MHz, and the radiation-pressure effect is found to be negligible for the reasons below. First, the magnitude of the bending moment and the proportional strain are zero at the irradiated position; this is discussed in more detail in Appendix B. In Appendix B, we also obtain an expression for the vertical deviation due to light pressure, which indicates that the magnitude of the deviation has an irradiation-position dependence. However, since the strain induced by

the cantilever occurs after a relatively long time delay, the response to the radiation pressure is time-averaged and is found to be only 0.3 nm for the maximum deviation. Second, for the pulse duration used (30 fs), the longitudinal force induced by the radiation pressure is 274 μN, which results in compression of the material. However, since the deformation area estimated from the characteristic longitudinal velocity of 6430 m/s [45] is only 0.2 nm, no strain due to bending of the cantilever occurs within the pulse duration (30 fs).

On the other hand, considering the effect of thermal expansion of the crystal lattice caused by a temperature rise as a photothermal effect, we find that a significant change in E_{ITT} is expected. If the length L of the cantilever is sufficiently large compared with its width w and thickness d, the lattice temperature T_l can be assumed to be uniform over the entire cross section, and the temperature field $T_l(x)$ at position x can be described by the one-dimensional thermal diffusion equation [46]. In our experiments, the temperature rise $\Delta T_l(x)$ can be evaluated by use of the following equation for bilayer cantilevers [47–50]:

$$\Delta T_l(x) = \frac{(1-R)P}{w(\lambda_{\mathrm{Al}} d_{\mathrm{Al}} + \lambda_{\mathrm{Si}} d_{\mathrm{Si}})} x, \tag{5}$$

where $d_{\mathrm{Al}} = 0.1$ μm and d_{Si} $(= d - d_{\mathrm{Al}})$ are the thicknesses of the Al and Si, respectively, and λ_{Al} and λ_{Si} are the thermal conductivities of Al and Si, respectively [47,48]. At a temperature of 300 K, $\lambda_{\mathrm{Al}} = 237\ \mathrm{W\,m^{-1}\,K^{-1}}$ [51] and $\lambda_{\mathrm{Si}} = 156\ \mathrm{W\,m^{-1}\,K^{-1}}$ [52]. From Eq. (5), the maximum of ΔT_l realized in this experiment is found to be approximately 474 K when the irradiation is done at the free end $(x = L)$ of the 240-μm cantilever. It is notable that the linear dependence of $A_{\mathrm{th}}(x)$ on the position x observed in our experimental results and the relationship between the cantilever thickness d and the rate of decrease of $A_{\mathrm{th}}(x)$ with respect to the position x can also be explained by using Eq. (5).

We estimate the change in E_{ITT} resulting from thermal expansion due to this temperature rise ΔT_l. Using a value for the coefficient of thermal expansion of Al at 300 K of 2.33×10^{-5}/K [53], the strain is found to be 1.1×10^{-2}. The relationship between the strain and ΔE_{ITT} for the Al film can be expressed using the deformation potential [54] dV_{200}/de as

$$\Delta E_{\mathrm{ITT}}(e) = 2\,\Delta V_{200}(e) = 2(dV_{200}/de)e. \tag{6}$$

The value of the deformation potential dV_{200}/de depends on the axiality of the strain [55]. Since thermal expansion is isotropic, −3.59 eV is used as the value of dV_{200}/de [55]. When the above distortion is applied in the equation, the resulting ΔE_{ITT} is −79 meV. This means that when the initial E_{ITT} is approximately 1.49 eV, it decreases to approximately 1.41 eV due to the temperature increase, and the inset of Fig. 4 shows that the value of ϵ_2 can be reduced by approximately 89% due to ΔE_{ITT}. Therefore, the large decrease in A_{th} is explained by the lattice distortion due to thermal expansion (photothermal effect), which causes a large shift in E_{ITT} and a significant decrease in the absorption due to interband transitions.

IV. SUMMARY

Using a microscopic femtosecond optical pump-probe technique, we observe the amplitudes of both the nonthermal and the thermalized electron signals from Al thin films on Si cantilevers. We find that the thermalized-electron-signal amplitude A_{th} varies linearly with the probe position, and A_{th} shows a significant drop at the free end of the cantilever. The unique position-dependent properties of the samples are explained by a change in the interband transition threshold ΔE_{ITT} caused by the position-dependent temperature rise and the associated thermal expansion caused by light absorption. In particular, the validity of our method is supported by the parallel band structure, which results in remarkable optical properties in Al, and the detection of small strains using extremely intense light, which can be realized only with a light source such as a femtosecond laser.

Furthermore, our method does not require the use of mechanical resonance of the cantilever for detecting radiation-pressure and photothermal effects. We argue that this study provides powerful measurement methods for various applications of cantilevers, such as in mechanical resonators [12,56], calorimetric sensors [47,48], and nanolithography [57,58]. Additionally, our findings provide useful insights into methods for measuring and controlling the optical properties of thin films [59] by exploiting the highly sensitive mechanical response of cantilevers. Moreover, further microscopic femtosecond optical pump-probe experiments on materials and microstructures are expected to lead to advanced ultrafast scanning probe microscopy systems.

ACKNOWLEDGMENTS

This work was supported by a Grant-in-Aid for Japan Society for the Promotion of Science (JSPS) Fellows (Grant No. 22J11423) and by Core Research for Evolutional Science and Technology (CREST), Japan Science and Technology Agency (JST) (Grant No. JPMJCR1875), Japan.

APPENDIX A: FITTING RESULTS FOR TRANSIENT REFLECTIVITY

The fitting parameters A_{th}, A_{NT}, τ_p, τ_{NT}, τ_{th}, and τ_{ep} are successfully extracted using Eq. (4). All coefficients used in the analysis are summarized in Table II. Here, A_0 is the value at the intercept $x = 0$ (the root of the cantilever), and

TABLE II. Coefficients (A_0, A_1) and standard deviations of the fitting parameters as a function of sampling position x by linear fitting ($A_0 + A_1 x$) for the time-domain signal from a cantilever L μm long.

	L (μm)	A_0	A_1
A_{NT}	160	$(971 \pm 6) \times 10^{-6}$	$(-3.03 \pm 0.06) \times 10^{-6}$
	200	$(796 \pm 6) \times 10^{-6}$	$(-2.44 \pm 0.06) \times 10^{-6}$
	240	$(779 \pm 12) \times 10^{-6}$	$(-2.72 \pm 0.09) \times 10^{-6}$
τ_p (fs)	160	36.4 ± 0.50	$(-3.24 \pm 0.54) \times 10^{-3}$
	200	36.1 ± 0.50	$(-4.74 \pm 0.44) \times 10^{-3}$
	240	37.2 ± 0.53	$(-2.17 \pm 0.39) \times 10^{-3}$
τ_{NT} (fs)	160	23.8 ± 0.10	$(3.18 \pm 1.09) \times 10^{-3}$
	200	22.9 ± 0.08	$(8.75 \pm 0.69) \times 10^{-3}$
	240	21.7 ± 0.17	$(15.8 \pm 1.22) \times 10^{-3}$
A_{th}	160	$(164 \pm 1.3) \times 10^{-6}$	$(-0.358 \pm 0.015) \times 10^{-6}$
	200	$(157 \pm 1.1) \times 10^{-6}$	$(-0.378 \pm 0.010) \times 10^{-6}$
	240	$(162 \pm 1.3) \times 10^{-6}$	$(-0.492 \pm 0.009) \times 10^{-6}$
τ_{th} (fs)	160	205 ± 1	$(154 \pm 15) \times 10^{-3}$
	200	198 ± 2	$(273 \pm 14) \times 10^{-3}$
	240	195 ± 1	$(316 \pm 11) \times 10^{-3}$
τ_{ep} (fs)	160	768 ± 7	$(548 \pm 80) \times 10^{-3}$
	200	792 ± 3	$(643 \pm 29) \times 10^{-3}$
	240	767 ± 5	$(438 \pm 39) \times 10^{-3}$

is comparable to the value obtained from an Al film on a stable substrate (see Sec. III A). A_1 is the slope of the line associated with the magnitude of the position dependence of the corresponding parameter. Although we discuss A_{th} in the main text, the other parameters A_{NT}, τ_p, τ_{NT}, τ_{th}, and τ_{ep} also show some position dependence, for which it is required to perform more experimental and theoretical analyses in the near future.

APPENDIX B: DERIVATION OF EQUATIONS FOR RADIATION PRESSURE AND STRAIN FOR A RECTANGULAR-SECTION CANTILEVER

In this appendix, we present an expression for the force F due to radiation pressure, the derivation of equations for the strain, and the deviation of the cantilever. The origin of the radiation pressure is the momentum of the pulsed photons, given by $\mathbf{p} = (E_i/c^2)\mathbf{v}$, where E_i is the energy of the incident light pulse, and $\mathbf{v}$ and c are the photon velocity and speed ($|\mathbf{v}| = c$), respectively [60,61]. From this equation, the momentum change in the direction of the z axis when light is incident on a medium with reflectivity R at an incidence angle θ is $\Delta p = (1 + R)\cos\theta\,(E_i/c)$. Since F is Δp divided by τ_p, and E_i is the time-averaged power P divided by f_{rep}, the above equation can be rewritten as

$$F = (1 + R)\cos\theta \frac{P}{c}\frac{1}{\tau_p f_{\mathrm{rep}}}. \tag{B1}$$

Equation (B1) can also be derived by using relations in which the absorptivity A is given by $A = 1 - R$ for a medium with a negligibly small transmittance, and the radiation pressure is expressed as the sum of an absorbed-light component (proportional to A) and a reflected-light component (proportional to $2R$), as $F = (2R + A)P/c$ [12]. Using Eq. (B1), F is calculated as 274 μN, given our experimental conditions ($R = 0.814$, $\theta = 45^\circ$, $P =$ 154 mW, $\tau_p = 30$ fs, and $f_{\mathrm{rep}} = 80$ MHz). This value of F is used in the main text. On the other hand, since the cantilever response (f_0, 73–280 kHz) is much slower than the repetition rate of the laser pulses (80 MHz), this force is time-averaged. The time-averaged force due to radiation pressure in the case of steady-state cantilever deflection is only about 0.7 nN, calculated by use of Eq. (B1) for $\tau_p f_{\mathrm{rep}} = 1$ (i.e., corresponding to cw light at 154 mW).

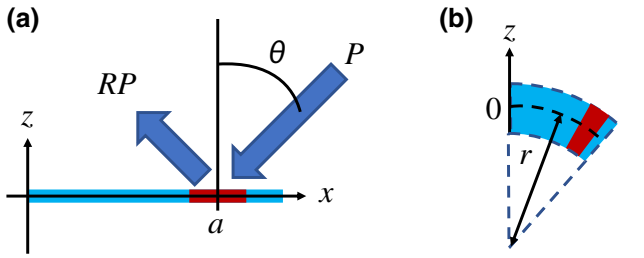

FIG. 5. (a) Description of the force on a cantilever (blue) due to radiation pressure caused by pulse irradiation and (b) the consequent bending. The irradiated position is marked in red on the blue area.

Next, we take the z axis in the thickness direction with the center of the cantilever as the origin and take the surface side as positive [displayed in Fig. 5(a)]. Here, the strain e as a function of z is $e(z) = z/r$, where r is the curvature of the cantilever [illustrated in Fig. 5(b)]. Based on a kinetic analysis for a rectangular-section cantilever [50,62], r is given by

$$\frac{1}{r} = \frac{M(x)}{YI}, \tag{B2}$$

where $M(x)$ is the bending moment, Y is the Young's modulus, and I is the area moment of inertia. When the light pressure occurs at the position $x = a$, the bending moment $M(x)$ is given by

$$M(x) = \begin{cases} F(a - x) & \text{for } x < a, \\ 0 & \text{for } x \geq a. \end{cases} \tag{B3}$$

For a rectangular-section cantilever, I is derived as

$$I = \frac{wd^3}{12}, \tag{B4}$$

where w and d are the width and thickness, respectively, of the cantilever. By solving for $e(z)$ using the above

equations, we obtain the following equation:

$$e(z) = \begin{cases} \dfrac{12F(a-x)}{Ywd^3}z & \text{for } x < a, \\ 0 & \text{for } x \geq a. \end{cases} \tag{B5}$$

Here, $x = a$ represents that the pump and probe beams are spatially overlapping. Except when $x < a$, $e(z)$ becomes zero, which means that there is no observable static strain, as discussed in previous sections.

Furthermore, expressing the deformation of the cantilever using the deviation in the z direction $\delta_z(x)$ as a function of x, in the case of small curvature r of the cantilever, the equation

$$\frac{1}{r} = \frac{\partial^2}{\partial x^2}\delta_z(x) \tag{B6}$$

is valid. Equations (B2) and (B6) allow us to formulate a differential equation for x. Under the conditions of Eq. (B3), the expression for $\delta_z(x)$ can be written as in the following equation:

$$\delta_z(x) = \begin{cases} \dfrac{2(3a-x)x^2}{Ywd^3}F & \text{for } x < a, \\ \dfrac{2(3x-a)a^2}{Ywd^3}F & \text{for } x \geq a. \end{cases} \tag{B7}$$

For $x = a$, this equation yields $\delta_z(x) = (4a^3F)/(Ywd^3)$, and the deviation is maximum when the cantilever is irradiated at the free end ($a = L$). Here, using the following equation for the spring constant k_z of the cantilever,

$$k_z = \frac{Ywd^3}{4L^3}, \tag{B8}$$

the maximum deviation can be calculated using $\delta_z(L) = F/k_z$. Therefore, the maximum deviation caused by the time-averaged radiation pressure in this experiment is 0.3 nm for $k_z = 2.2$ N/m, for the 240-μm-long cantilever, and we believe that the effect of deformation due to the time-averaged radiation pressure at any position of the cantilever is negligibly small.

APPENDIX C: DERIVATION OF EQUATIONS FOR TEMPERATURE RISE IN A RECTANGULAR-SECTION CANTILEVER

Since heat conduction in a cantilever depends on its material and shape, to obtain an accurate temperature distribution, it is necessary to solve the three-dimensional diffusion equation by the finite-element method [63,64]. On the other hand, if the length L of the cantilever is sufficiently large compared with its width w and thickness d, the temperature T can be assumed to be uniform over the entire cross section, and the temperature distribution can be described by the one-dimensional thermal diffusion equation as

$$\rho C_l \frac{\partial T}{\partial t} - \frac{\partial}{\partial x}\left[\lambda(T)\frac{\partial T}{\partial x}\right] = q(x), \tag{C1}$$

where ρ is the mass density, λ is the thermal conductivity at the temperature T, and q is the density of heat sources or sinks at the position x [46]. In our measurements, the characteristic time of heat conduction $\rho C_l L^2/\lambda$ is on a submillisecond scale, which is much longer than the repetition period of the pulsed light (12.5 ns) and much shorter than the integration time (greater than 100 s). Therefore, the temperature distribution generated by repeated pulse irradiation can be regarded as stationary ($dT/dt = 0$) [46]. Furthermore, we assume that the heat transfer to the ambient environment is negligibly small compared with the heat conduction in the cantilever. The surfaces of the cantilever are assumed to be thermally insulated except at the heated point a, and then Eq. (C1) is transformed as follows:

$$\frac{\partial}{\partial x}\left[\lambda(T)\frac{\partial T}{\partial x}\right] = \frac{(1-R)P}{wd}\delta_D(x-a), \tag{C2}$$

where δ_D is the Dirac distribution. The distribution of the temperature rise $\Delta T_l(x) = T_l(x) - T_0$ can be obtained by integrating Eq. (C2) twice under boundary conditions assuming isothermally clamped ends [$T_l(x = 0) = T_0$] and thermally insulated free ends ($[dT_l/dx]_{x=L} = 0$), as

$$\begin{cases} \displaystyle\int_{T_0}^{T_0+\Delta T_l} \lambda(T')\,dT' = \frac{(1-R)P}{wd}x & \text{for } x \leq a, \\ \Delta T_l(x) = \Delta T_l(a) & \text{for } x > a. \end{cases} \tag{C3}$$

If $\lambda(T)$ is a constant, i.e., $\lambda(T) = \lambda_0$, the integral can be evaluated as

$$\Delta T_l(x) = \frac{(1-R)P}{w\lambda_0 d}x \tag{C4}$$

for $x \leq a$ [46]. This equation can be extended to an expression applicable to a bilayer cantilever [47–50] by replacing λ_0 and d with the values for the respective layers, and an equation adapted to our experimental conditions is obtained as in Eq. (5). This temperature rise causes significant thermal expansion, but does not exceed the melting point of Al (approximately 933 K). The temperature dependence of λ leads to the temperature distribution being nonlinear [46], but our experimental results do not show a nonlinear trend, because the value to which the temperature rises (300 + 474 K) is smaller than the melting point of Al. Other factors involved in modifying the model (e.g., boundary-condition issues) are beyond the scope of this paper.

[1] T. Qiu and C. Tien, Short-pulse laser heating on metals, Int. J. Heat Mass Transf. **35**, 719 (1992).

[2] A. Ashkin, Acceleration and Trapping of Particles by Radiation Pressure, Phys. Rev. Lett. **24**, 156 (1970).

[3] S. L. Jacques, Laser-tissue interactions: Photochemical, photothermal, and photomechanical, Surg. Clin. North Am. **72**, 531 (1992).

[4] S. Yoshida, Y. Kanitani, R. Oshima, Y. Okada, O. Takeuchi, and H. Shigekawa, Microscopic Basis for the Mechanism of Carrier Dynamics in an Operating *p-n* Junction Examined by Using Light-Modulated Scanning Tunneling Spectroscopy, Phys. Rev. Lett. **98**, 026802 (2007).

[5] Y. Terada, S. Yoshida, O. Takeuchi, and H. Shigekawa, Real-space imaging of transient carrier dynamics by nanoscale pump–probe microscopy, Nat. Photonics **4**, 869 (2010).

[6] J. C. Maxwell, *A Treatise on Electricity and Magnetism* (Clarendon Press, Oxford, 1873), Vol. 1.

[7] E. F. Nichols and G. F. Hull, The pressure due to radiation, Proc. Am. Acad. Arts Sci. **38**, 559 (1903).

[8] P. Musen, The influence of the solar radiation pressure on the motion of an artificial satellite, J. Geophys. Res. **65**, 1391 (1960).

[9] M. Ziebart and P. Dare, Analytical solar radiation pressure modelling for GLONASS using a pixel array, J. Geod. **75**, 587 (2001).

[10] K. Yamamoto, *et al.*, Dynamic precise orbit determination of Hayabusa2 using laser altimeter (LIDAR) and image tracking data sets, Earth Planets Space **72**, 85 (2020).

[11] D. Gao, W. Ding, M. Nieto-Vesperinas, X. Ding, M. Rahman, T. Zhang, C. Lim, and C.-W. Qiu, Optical manipulation from the microscale to the nanoscale: Fundamentals, advances and prospects, Light Sci. Appl. **6**, e17039 (2017).

[12] D. Ma, J. L. Garrett, and J. N. Munday, Quantitative measurement of radiation pressure on a microcantilever in ambient environment, Appl. Phys. Lett. **106**, 091107 (2015).

[13] M. Allegrini, C. Ascoli, P. Baschieri, F. Dinelli, C. Frediani, A. Lio, and T. Mariani, Laser thermal effects on atomic force microscope cantilevers, Ultramicroscopy **42–44**, 371 (1992).

[14] D. R. Evans, P. Tayati, H. An, P. K. Lam, V. S. J. Craig, and T. J. Senden, Laser actuation of cantilevers for picometre amplitude dynamic force microscopy, Sci. Rep. **4**, 5567 (2014).

[15] S. Yoshida, Y. Aizawa, Z.-H. Wang, R. Oshima, Y. Mera, E. Matsuyama, H. Oigawa, O. Takeuchi, and H. Shigekawa, Probing ultrafast spin dynamics with optical pump–probe scanning tunnelling microscopy, Nat. Nanotechnol. **9**, 588 (2014).

[16] R. H. M. Groeneveld, R. Sprik, and A. Lagendijk, Femtosecond spectroscopy of electron-electron and electron-phonon energy relaxation in Ag and Au, Phys. Rev. B **51**, 11433 (1995).

[17] E. Carpene, Ultrafast laser irradiation of metals: Beyond the two-temperature model, Phys. Rev. B **74**, 024301 (2006).

[18] E. Beaurepaire, J.-C. Merle, A. Daunois, and J.-Y. Bigot, Ultrafast Spin Dynamics in Ferromagnetic Nickel, Phys. Rev. Lett. **76**, 4250 (1996).

[19] J.-Y. Bigot, M. Vomir, and E. Beaurepaire, Coherent ultrafast magnetism induced by femtosecond laser pulses, Nat. Phys. **5**, 515 (2009).

[20] A. J. Sabbah and D. M. Riffe, Femtosecond pump-probe reflectivity study of silicon carrier dynamics, Phys. Rev. B **66**, 165217 (2002).

[21] W. Z. Lin, L. G. Fujimoto, E. P. Ippen, and R. A. Logan, Femtosecond carrier dynamics in GaAs, Appl. Phys. Lett. **50**, 124 (1987).

[22] W. Z. Lin, J. G. Fujimoto, E. P. Ippen, and R. A. Logan, Femtosecond dynamics of highly excited carriers in $Al_xGa_{1-x}As$, Appl. Phys. Lett. **51**, 161 (1987).

[23] M. I. Kaganov, Relaxation between electrons and the crystalline lattice, Sov. Phys. JETP **4**, 173 (1957).

[24] P. B. Allen, Theory of Thermal Relaxation of Electrons in Metals, Phys. Rev. Lett. **59**, 1460 (1987).

[25] C.-K. Sun, F. Vallée, L. Acioli, E. P. Ippen, and J. G. Fujimoto, Femtosecond investigation of electron thermalization in gold, Phys. Rev. B **48**, 12365 (1993).

[26] M. Hase, K. Ishioka, J. Demsar, K. Ushida, and M. Kitajima, Ultrafast dynamics of coherent optical phonons and nonequilibrium electrons in transition metals, Phys. Rev. B **71**, 184301 (2005).

[27] U. Ritzmann, P. M. Oppeneer, and P. Maldonado, Theory of out-of-equilibrium electron and phonon dynamics in metals after femtosecond laser excitation, Phys. Rev. B **102**, 214305 (2020).

[28] H. Hirori, T. Tachizaki, O. Matsuda, and O. B. Wright, Electron dynamics in chromium probed with 20-fs optical pulses, Phys. Rev. B **68**, 113102 (2003).

[29] X. Shen, Y. P. Timalsina, T.-M. Lu, and M. Yamaguchi, Experimental study of electron-phonon coupling and electron internal thermalization in epitaxially grown ultrathin copper films, Phys. Rev. B **91**, 045129 (2015).

[30] J. Hohlfeld, S.-S. Wellershoff, J. Güdde, U. Conrad, V. Jähnke, and E. Matthias, Electron and lattice dynamics following optical excitation of metals, Chem. Phys. **251**, 237 (2000).

[31] P. Maldonado, T. Chase, A. H. Reid, X. Shen, R. K. Li, K. Carva, T. Payer, M. Horn von Hoegen, K. Sokolowski-Tinten, X. J. Wang, P. M. Oppeneer, and H. A. Dürr, Tracking the ultrafast nonequilibrium energy flow between electronic and lattice degrees of freedom in crystalline nickel, Phys. Rev. B **101**, 100302(R) (2020).

[32] J.-W. Kim, M. Vomir, and J.-Y. Bigot, Ultrafast Magnetoacoustics in Nickel Films, Phys. Rev. Lett. **109**, 166601 (2012).

[33] Y. Murakami, P. Werner, N. Tsuji, and H. Aoki, Interaction quench in the Holstein model: Thermalization crossover from electron- to phonon-dominated relaxation, Phys. Rev. B **91**, 045128 (2015).

[34] A. F. Kemper, M. A. Sentef, B. Moritz, J. K. Freericks, and T. P. Devereaux, Effect of dynamical spectral weight redistribution on effective interactions in time-resolved spectroscopy, Phys. Rev. B **90**, 075126 (2014).

[35] K. F. MacDonald, Z. L. Sámson, M. I. Stockman, and N. I. Zheludev, Ultrafast active plasmonics, Nat. Photonics **3**, 55 (2009).

[36] X. Chen, D. Hu, R. Mescall, G. You, D. N. Basov, Q. Dai, and M. Liu, Modern scattering-type scanning near-field optical microscopy for advanced material research, Adv. Mater. **31**, 1804774 (2019).
[37] W. A. Harrison, Parallel-band effects in interband optical absorption, Phys. Rev. **147**, 467 (1966).
[38] H. Ehrenreich, H. R. Philipp, and B. Segall, Optical properties of aluminum, Phys. Rev. **132**, 1918 (1963).
[39] N. W. Ashcroft and K. Sturm, Interband absorption and the optical properties of polyvalent metals, Phys. Rev. B **3**, 1898 (1971).
[40] G. Meyer and N. M. Amer, Novel optical approach to atomic force microscopy, Appl. Phys. Lett. **53**, 1045 (1988).
[41] Z. Lin, L. V. Zhigilei, and V. Celli, Electron-phonon coupling and electron heat capacity of metals under conditions of strong electron-phonon nonequilibrium, Phys. Rev. B **77**, 075133 (2008).
[42] F. Cheng, P.-H. Su, J. Choi, S. Gwo, X. Li, and C.-K. Shih, Epitaxial growth of atomically smooth aluminum on silicon and its intrinsic optical properties, ACS Nano. **10**, 9852 (2016).
[43] R. W. Schoenlein, W. Z. Lin, J. G. Fujimoto, and G. L. Eesley, Femtosecond Studies of Nonequilibrium Electronic Processes in Metals, Phys. Rev. Lett. **58**, 1680 (1987).
[44] F. Szmulowicz and B. Segall, Calculation of optical spectra of aluminum, Phys. Rev. B **24**, 892 (1981).
[45] M. Grossmann, M. Schubert, C. He, D. Brick, E. Scheer, M. Hettich, V. Gusev, and T. Dekorsy, Characterization of thin-film adhesion and phonon lifetimes in Al/Si membranes by picosecond ultrasonics, New J. Phys. **19**, 053019 (2017).
[46] B. Pottier, F. Aguilar Sandoval, M. Geitner, F. Esteban Melo, and L. Bellon, Silicon cantilevers locally heated from 300 K up to the melting point: Temperature profile measurement from their resonances frequency shift, J. Appl. Phys. **129**, 184503 (2021).
[47] C. Canetta and A. Narayanaswamy, Sub-picowatt resolution calorimetry with a bi-material microcantilever sensor, Appl. Phys. Lett. **102**, 103112 (2013).
[48] J. R. Barnes, R. J. Stephenson, C. N. Woodburn, S. J. O'Shea, M. E. Welland, T. Rayment, J. K. Gimzewski, and C. Gerber, A femtojoule calorimeter using micromechanical sensors, Rev. Sci. Instrum. **65**, 3793 (1994).
[49] S. Shen, A. Narayanaswamy, S. Goh, and G. Chen, Thermal conductance of bimaterial microcantilevers, Appl. Phys. Lett. **92**, 063509 (2008).
[50] D. Ramos, J. Mertens, M. Calleja, and J. Tamayo, Study of the origin of bending induced by bimetallic effect on microcantilever, Sensors **7**, 1757 (2007).
[51] G. K. White and M. L. Minges, Thermophysical properties of some key solids: An update, Int. J. Thermophys. **18**, 1269 (1997).
[52] C. J. Glassbrenner and G. A. Slack, Thermal conductivity of silicon and germanium from 3 K to the melting point, Phys. Rev. **134**, A1058 (1964).
[53] K. Wang and R. Reeber, The perfect crystal, thermal vacancies and the thermal expansion coefficient of aluminium, Philos. Mag. A **80**, 1629 (2000).
[54] P. Y. Yu and M. Cardona, *Fundamentals of Semiconductors: Physics and Materials Properties* (Springer, Berlin, Heidelberg, 1996).
[55] D. Jiles, Pseudopotential coefficients for the electron band structure of aluminium and their deformation potentials from piezoreflectance measurements, Solid State Commun. **51**, 327 (1984).
[56] D. Kleckner and D. Bouwmeester, Sub-kelvin optical cooling of a micromechanical resonator, Nature **444**, 75 (2006).
[57] P. E. Sheehan, L. J. Whitman, W. P. King, and B. A. Nelson, Nanoscale deposition of solid inks via thermal dip pen nanolithography, Appl. Phys. Lett. **85**, 1589 (2004).
[58] A. A. Milner, K. Zhang, and Y. Prior, Floating tip nanolithography, Nano Lett. **8**, 2017 (2008).
[59] R. Roldán, A. Castellanos-Gomez, E. Cappelluti, and F. Guinea, Strain engineering in semiconducting two-dimensional crystals, J. Phys. Condens. Matter **27**, 313201 (2015).
[60] I. S. Grant and W. R. Phillips, *Electromagnetism* (Wiley, Chichester, 1990), 2nd ed.
[61] U. S. Inan, A. S. Inan, and R. K. Said, *Engineering Electromagnetics and Waves* (Pearson, Boston, 2014), 2nd ed.
[62] D. Sarid, *Exploring Scanning Probe Microscopy with MATHEMATICA* (Wiley-VCH, Weinheim, 2006), 2nd ed.
[63] B. A. Bircher, L. Duempelmann, H. P. Lang, C. Gerber, and T. Braun, Photothermal excitation of microcantilevers in liquid: Effect of the excitation laser position on temperature and vibrational amplitude, Micro Nano Lett. **8**, 770 (2013).
[64] A. A. Milner, K. Zhang, V. Garmider, and Y. Prior, Heating of an atomic force microscope tip by femtosecond laser pulses, Appl. Phys. A **99**, 1 (2010).